Biomicrofluidics
July 2022, Volume 16 Issue 4 Pages 044111 (??p.)
https://doi.org/10.1063/5.0073542
https://archimer.ifremer.fr/doc/00791/90254/

Hybridization-based DNA biosensing with a limit of detection of 4 fM in 30 s using an electrohydrodynamic concentration module fabricated by grayscale lithography

Tijunelyte Inga [1], Teillet Jeffrey [1], Bruand Paul [1], Courson Remi [1], Lecestre Aurélie [1], Joseph Pierre [1], Bancaud Aurélien [1, *]

[1] CNRS, LAAS, 7 avenue du colonel Roche, F-31400 Toulouse, France

* Corresponding author : Aurélien Bancaud, email address : abancaud@laas.fr

Abstract :

Speeding up and enhancing the performances of nucleic acid biosensing technologies have remained drivers for innovation. Here, we optimize a fluorimetry-based technology for DNA detection based on the concentration of linear targets paired with probes. The concentration module consists of a microfluidic channel with the shape of a funnel in which we monitor a viscoelastic flow and a counter-electrophoretic force. We report that the technology performs better with a target longer than 100 nucleotides (nt) and a probe shorter than 30 nt. We also prove that the control of the funnel geometry in 2.5D using grayscale lithography enhances sensitivity by 100-fold in comparison to chips obtained by conventional photolithography. With these optimized settings, we demonstrate a limit of detection of 4 fM in 30 s and a detection range of more than five decades. This technology hence provides an excellent balance between sensitivity and time to result.

Keywords : Electrohydrodynamic concentration, fluorescence sensor, microfluidics, grayscale lithograph

INTRODUCTION

The worldwide Covid-19 crisis has brought nucleic acid biosensing technologies, particularly the quantitative real-time reverse-transcriptase polymerase chain reaction (qRT-PCR), to the headlines. Enzymatic amplification technologies are the most sensitive with reported limits of detection (LoD) of ~10^3 copies of viral RNA per milliliter of body fluids [1,2], or equivalently attoMolar concentrations. Considerable efforts have been made to reduce the total analytical time down to 30 minutes, including the purification of nucleic acids prior to amplification[3]. These impressive achievements have complicated the development of competitive amplification-free technologies [4], which nevertheless remain a driving research direction in the field of bioengineering [5,6].

Amplification-free detection technologies can be roughly cast into two categories depending on whether detection occurs in bulk or on surfaces. Commonly based on mass, electrical, or optical index variation, surface detection strategies reach fM performances [7,8]. The highest sensitivities are generally obtained with nanosensors, which are not competitive in terms of time to response due to the overly long target:probe interaction kinetics limited by diffusion[9]. Using an electric field to drive the targets towards the sensor electrophoretically showed a good compromise between the sensitivity of 30 fM and detection time of 15 minutes [10]. The trade-off is usually the opposite in bulk assays given that nucleic acids detection is rapid but the sensitivity is low. For instance, using a molecular beacon (MB) probe, which changes conformation and becomes fluorescent upon hybridization to the target, the LoD of 1 nM can be reached within 20 to 60 min [11]. However, this approach usually leads to a low dynamic range due to the background signal from unreacted MBs [12]. Strand displacement reactions have been integrated into the detection scheme to associate DNA hybridization events with a subsequent cascade of detectable readouts [13,14]. These assays attained sub-pM to sub-fM LoDs [15–18], though generally also at the expense of a long time to result [19]. In another yet non-mutually exclusive direction, a compromise between fast and sensitive detection has been reached with concentration modules. Using conventional MB and isotachophoresis for concentration, an LoD of 5 pM in 3 minutes has been reported [20–22]. In line with this biosensing technology based on a concentration module, we recently developed the µLAS technology (µ-Laboratory for DNA analysis and separation), which enables DNA size separation, concentration, and purification in a microchannel using bi-

directional electrohydrodynamic actuation [23–26]. This technology has been exploited to detect nucleic acids by the selective concentration of the complex formed between the target molecule and a complementary MB [27]. We reported an LoD of 2 pM within 30 seconds. Here, after a description of the operating conditions of the technology, we enhance its biosensing performances by optimizing the microfluidic chip geometry and the target:probe size settings. Specifically, 2.5D microchannels are fabricated by direct grayscale lithography (GSL) to produce funnel shaped geometries with non-uniform width and height. GSL has already been used in microfluidics to obtain complex free-standing shapes[28] or design programmable gradients[29], valves[30], and model porous systems[31], but to the best of our knowledge, it has not been applied to design biosensing systems. An LoD of 4 fM in 30 seconds is achieved with these GSL chips. This performance is comparable to the level detection achieved by nanosensors [7,8], though the production of our devices is greatly simplified. Moreover, it constitutes a good trade-off between sensitivity and time to result since detection at 0.1 fM typically takes 10 minutes.

MATERIALS AND METHODS

Materials and reagents

Chemicals were purchased from Signa-Aldrich, unless mentioned. The neutral polymer polyvinylpyrrolidone (PVP; MW=1.3 MDa) was dissolved in water at 6% (w:v) concentration. This stock solution was mixed with PBS (Dulbecco's Phosphate buffer saline) to obtain a PVP concentration of 5% and 22 mM of NaCl. The viscosity and viscoelastic relaxation time of the solution were 31 mPa.s and 1.1 ms, respectively, as evaluated using the technique described in [32]. Note that (i) PVP was chosen due to its minimal shear-thinning behavior [33], and (ii) the addition of salt allowed us to increase the fluorescence signal in comparison to electrophoresis buffers (Supplementary Fig. S1). Prior to use, all solutions were filtered with 0.2 µm filters.

Genomic material

Four oligonucleotides were obtained from Eurogentec (Belgium), dissolved in Tris-HCl 10 mM and EDTA 1 mM (pH = 7.5) at a stock concentration of 100 µM, and stored at -20°C:

Short probe (SP, 22 nt)	5'-6-FAM-TCA-ACA-TCA-GTC-TGA-TAA-GCT-A-3'
Long probe (LP, 98 nt)	5'-6-FAM- A_{38}-TCA-ACA-TCA-GTC-TGA-TAA-GCT-A_{38}-3'
Short target (ST, 22 nt)	5'-TAG-CTT-ATC-AGA-CTG-ATG-TTG-A-3'
Long target (LT, 92 nt)	5'- A_{35}-TAG-CTT-ATC-AGA-CTG-ATG-TTG-A-A_{35}-3'

6-FAM corresponds to 6-carboxyfluorescein. Further in the text, we use four complexes, namely SP:ST, LP alone, SP:LT, and LP:ST, that we define as the targets of 44, 98, 114, and 120 nt, respectively. Nucleic acid samples were prepared as follows: (i) the stock of probe and target were diluted in 1X-DPBS at 1 µM; (ii) 1 µL of target and 1 µL of the probe were then mixed, heated at 92°C for 5 min, and cooled down to RT; (iii) PVP based buffer was added to obtain the final probe:target complex concentration. The solution was then extensively vortexed for three minutes and left at room temperature to homogenize for one hour. For calibration experiments, we used a constant probe concentration of 100 nM and diluted the target by consecutive increments of 10-fold before heating to obtain concentrations spanning 20 nM to 20 fM.

2D and 2.5D microfluidic chips

The microfluidic chips with a uniform height of 2, 4, or 6 µm were obtained by conventional photolithography with the protocol described in [23]. Grayscale lithography chips were processed after improving the protocol of [31]. The silicon wafer was first submitted to 800 W O_2 plasma for 5 min to promote the adhesion of a 1.1 µm layer of the photoresist AZ ECI 3012 (Microchemicals GmbH) spin-coated at 3600 rpm with an acceleration of 5000 rpm/s. Exposure was operated by laser lithography (Dilase 750, Kloé SA) using a fixed 405 nm laser diode and translating the wafer along lines. The laser beam was focused by a 10X objective (numerical aperture, NA=0.3) to produce a spot diameter of ~20 µm. The 100 mW laser beam was attenuated to 10 %, and further modulated by increments of 0.1 % in the range from 10 to 50% (Supplementary Fig. S2). After exposure, the resist was baked at 126 °C for 5 min and finally developed in MFCD-26 solution for 30 s. The maximal and minimal depths of the resulting 2.5D structures were 0.5±0.09 and 1.05±0.07 µm, respectively (Supplementary Fig. S2). These

patterns were eventually transferred into silicon by plasma etching, producing gradients from 1.9±0.2 to 5.2±0.1 µm. The etching selectivity, as defined by the ratio of silicon to photoresist transferred depth, was 5 for a plasma etching process time of 22 min.

Fabricated chips were then placed in a custom chip support with inlet and outlet reservoirs sealed by O-rings (Supplementary Fig. S3). The reservoirs contained 0.5 mm diameter platinum wires (GoodFellow) as electrodes. Actuation was operated with a 7 bar pressure controller (Fluigent) and a DC high voltage power supply (Labsmith). Before each experiment, microfluidic chips were filled with ethanol to eliminate air bubbles, then flushed with milli-Q water, and subsequently filled with the PVP working buffer. Finally, the sample solutions containing genomic material were introduced into the chip, and analysis was carried out for one minute. The chip was extensively rinsed with the PVP working buffer between each analysis.

Microscopy and image analysis

Data were acquired using Leica fluorescence microscopes equipped with light engines for cyan excitation (Lumencore), and sCMOS digital cameras from Hamamatsu. 20X air objective (NA=0.8) was used. For time-lapse video acquisitions, the inter-frame interval was set to 2 s with an exposure time of 0.1 s and a binning of 4x4 (512*152 pixels of 1.3 µm in size). The resulting videos were processed using the Fiji software [34]. The position of stagnation of the cloud of concentrated molecules was inferred by measuring the distance to the constriction of its center of mass. In order to extract the LoD, we used the method described in ref. [27]. Briefly, we recorded 10 images before the application of the electric field, and used the corresponding intensity signal to define the background and its standard deviation. For titration, we first applied a 4x4 binning filter, and then measured the fluorescence signal next to the constriction using a region of interest (ROI) selected as a 200 µm line of 5 µm thickness. The fluorescence intensity profile was fitted with a Gaussian to retrieve the maximum intensity. Finally, the maximum intensities were plotted as a function of concentration, and the LoD was obtained by extrapolation of the signal to two times the standard deviation of the background. Data fitting was performed using power-law and Gaussian functions in Igor-Pro.

COMSOL simulations

Finite element simulations were run with COMSOL Multiphysics 5.6. We used AC/DC electric current and Computational Fluid Dynamics modules assuming laminar flow. The fluid conductivity was set to 0.24 S/m and the viscosity to 31 mPa.s. Boundary conditions consisted of electrical isolation and no flux at the lateral walls of the chip (see drawing in Supplementary Materials). An electric potential difference of 100 V and a pressure difference of 1 bar were set between the inlet and outlet to compute the maximum electric field and flow velocity.

RESULTS & DISCUSSION

Operation of the concentration module

In a 2D microfluidic funnel of maximal and minimal width *W* and *w*, respectively (Fig. 1A), the hydrodynamic flow velocity at the centerline of the channel typically ranges from $v_0^{max} \times w/W$ to v_0^{max}, according to mass conservation laws, and similarly, the electric field spans $E^{max} \times w/W$ to E^{max}. Given that v_0^{max} is typically 50 mm/s (Table 1), the Reynold number is ~0.01 and the flow is laminar. The use of electric fields neither induces detectable temperature change in the silicon chip nor does it alter DNA hybridization reactions, as we showed in ref. [27].

The funnel shape is reminiscent of the geometry of dielectrophoretic trapping modules [35–37]. Our actuation strategy is however very different because we apply continuous electric fields and dielectrophoretic trapping is most frequently based on high-frequency electric fields. Notably, a few contributions described DNA concentration by Direct Current insulator-based gradient dielectrophoresis [38–40], but the size of funnels of less than 100 nm and the elimination of hydrodynamic forces to achieve concentration cannot be compared to our experimental settings. Thus, we claim that DNA trapping in our module is enabled by a transverse force F_{VE} perpendicular to the flow direction and oriented toward the upper and lower walls (shown in the (xz) plane of Fig. 1A). We use a salty and viscoelastic solution (see Methods), implying that F_{VE} arises from the variation of the normal stress in the gradient direction [41], rather than from hydrodynamic interactions around DNA created by the electric field [42]. As we showed in ref. [43], this force F_{VE} can be expressed analytically with a linear dependence on the hydrodynamic and electric field v_0 and E:

$$\overrightarrow{F_{VE}}(z) \sim -\frac{N}{h} \times v_0 \times E \times (1 - 2\frac{z}{h}) \times \overrightarrow{u_z} \quad (1)$$

with z the distance from the lower wall in Fig. 1A, N the size of the molecule, h the channel height and $\overrightarrow{u_z}$ the unit vector. Note that this transverse force depends on the equilibrium end-to-end distance of the chain N because hydrodynamic interactions are screened out in viscoelastic solutions and the Rouse model applies, as shown in ref. [43]. Fluctuations of the length of the molecules during their migration are discussed in ref. [41].

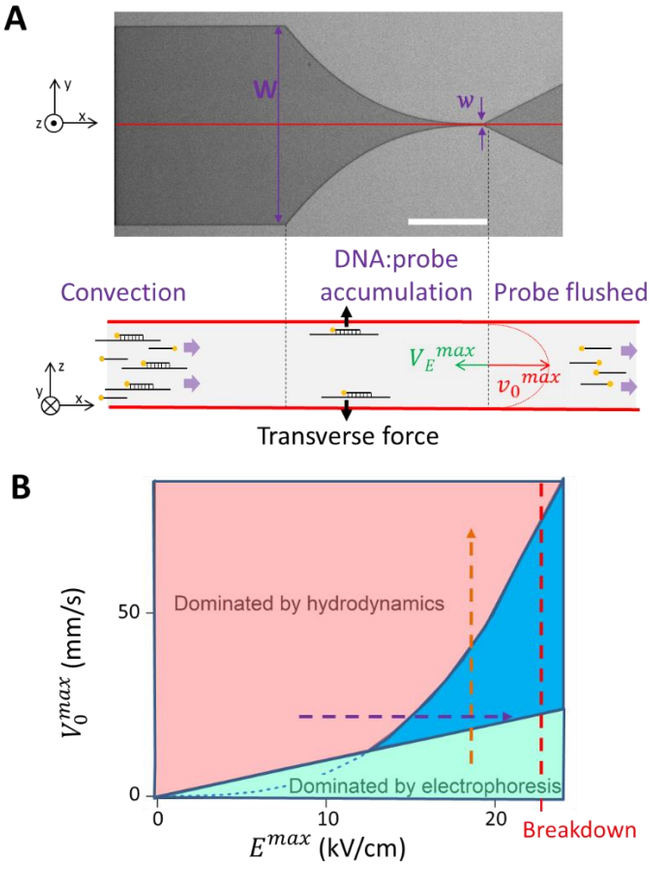

Figure 1. Principle of the biosensing module. (A) *The optical micrograph shows one microfluidic chip in the (xy) plane. The funnel maximum and minimal width W and w, respectively, are represented. The symmetry axis of the channel is highlighted by a red line, and the response of DNA molecules along this line in the (xz) plane is represented below. The hydrodynamic flow field is oriented along the x-axis and characterized by a Poiseuille profile in the xz plane (red arrow). The electrophoretic force is oriented in the opposite direction with a flat profile in the (xz) plane (green arrow). The scale bar corresponds to 200 µm.* ***(B)*** *Actuation parameter space of the concentration module as deduced from the model. Concentration occurs in the blue sector. Silicon oxide breakdown reduces the operating range in electric field (red dashed line), the maximum tension that can be applied in these*

chips is in the range of 200 to 300 V. Optimization of detection performances is either performed by increasing tension at constant pressure or by increasing pressure at constant tension (purple and orange arrows, respectively).

Eq. (1) is valid for molecules far from the wall because it is derived by the reflection method [43]. In ref. [43], we suggested an extrapolation for the force profile, considering that additional repulsive forces, including electrostatic and/or shear-induced electroviscous forces [44] and/or lubrication [45] forces, balance the viscoelastic transverse force. The resulting effective force vanishes toward the wall, and may be approximated by a linear drop, following the expression:

$$\overrightarrow{F_{wall}}(z) \sim -N \times v_0 \times E \times \frac{z}{h^2} \times \overrightarrow{u_z} \qquad (2)$$

Note that expression (2) is valid for the lower wall in Fig. 1A. Predictions based on this model have been successfully confronted to an extensive set of more than 300 data in ref. [43].

Let us now define the regime of operation of the concentration module. Far upstream from the constriction, hydrodynamic and electrophoretic velocities are low, and the transverse force can be neglected. Molecules reach the concentration module if the average flow velocity is greater than the electrophoretic velocity, equivalently $v_0^{max} > 2\mu_0 E^{max}$ with μ_0 the electrophoretic mobility. The sector represented in green in Fig. 1B corresponds to $v_0^{max} < 2\mu_0 E^{max}$. As molecules migrate toward the funnel, electrophoretic and hydrodynamic velocities increase, and so does F_{wall}. The concentration module operates if the regime of migration is dominated by electrophoresis at the apex of the funnel. Applying Boltzmann statistics to the transverse force in Eq. (2), we infer the average distance of the molecules to the wall $\langle z_{DNA} \rangle$ that scales as $(N v_0 E/h^2)^{-0.5}$. Linearizing the expression of the flow velocity near the bottom wall $4v_0^{max}\langle z_{DNA}\rangle/h$, the condition of dominant electrophoretic migration at the apex reads

$$v_0^{max} < \frac{N{\mu_0}^3}{16} \times E^{max3} \qquad (3)$$

If this condition is unfulfilled, the migration is dominated by hydrodynamics everywhere in the concentration module, and the corresponding sector is depicted in red in Fig. 1B. In the light blue sector, hydrodynamic forces prevail over electrophoresis at the entry of the funnel whereas electrophoresis is predominant at the tip of the apex. Hence, one position of balanced electrophoretic and hydrodynamic forces exists along the funnel, and hybridized DNA molecules,

continuously conveyed toward, accumulate at this stagnation position. Moreover, unbound probes, which have a smaller molecular weight than the target:probe complex, undergo transverse forces of lower amplitude. They can thus be flushed out, and selective target detection is achieved, as was demonstrated in ref. [27]. Notably, the resulting theoretical diagram is in qualitative agreement with that reported in ref. [46] based on experimental measurements of high MW genomic DNA.

Chip geometry	2 µm	4 µm	6 µm	GSL
Hydraulic resistance (10^{16} kg/m^{4}s)	27.4	3.6	1.1	19.5
Electric resistance (MOhm)	13.8	7.9	5.9	12.0
v_0^{max} (mm/s)	37 (@ 5 bar)	57 (@ 2 bar)	61 (@1 bar)	51 (@5 bar)
E^{max} (kV/cm)	23 (@ 290 V)	20 (@ 290 V)	12 (@290 V)	17 (@190 V)

Table 1. *Electrohydrodynamic parameters for the microfluidic chip geometries used in this study as deduced from finite element simulations (see Methods).*

Optimization of the concentration module

The phase diagram in Fig. 1B can be investigated experimentally by applying a constant electric field and gradually increasing hydrodynamic forces, or using a constant pressure and increasing the electric field (orange and purple arrows in Fig. 1B, respectively). We first report an experiment performed in a chip of 2 µm in height (Fig. 2A), in which v_0^{max} is set to 30 mm/s and E^{max} is increased stepwise. For each step indicated by the green dashed lines in Fig. 2A, the position of stagnation shifts away from the constriction (see the selected snapshots recorded at times t_1, t_2 and t_3). Below 21.5 kV/cm, each electric field step is associated with an increase in the maximum intensity (Fig. 2B). At 22 kV/cm and above, the maximum intensity signal decreases, but the total fluorescence signal still rises (Supplementary Fig. S4). This experiment shows that the concentration module is optimal for a set of electrohydrodynamic actuation parameters, which correspond to E^{max} of ~21 kV/cm with this microchip geometry. The result is confirmed by the mirror experiment that consists in increasing the pressure at constant electric field while recording fluorescence intensity in the funnel (Fig. 2C; this corresponds to the orange arrow in

the diagram of Fig. 1B). The signal is initially null in the concentration module because the migration is dominated by electrophoresis. Fluorescence intensity then increases to reach an optimum for v_0^{max} of ~2.3, 2.9, and 3.1 cm/s depending on the salt concentration in the solution, and decreases due to the leaks associated with a regime of concentration dictated by prevalent hydrodynamic forces.

The kinetics of molecular accumulation can be used as a readout to optimize the performance of the concentration module. The inset of Fig. 2B shows that the typical timescale of concentration increases from 1 to 10 s as E^{max} increases from 16 kV/cm to 21 kV/cm, respectively. The saturation of the signal after the concentration phase is explained by the occurrence of velocity fluctuations around the stagnation position, as described in ref.[41,43]. For a low electric field, the stagnation position is close to the apex, and fluctuations are likely to disengage T:P from the concentration module. The onset of the electric field forces T:P complexes to shift away from the constriction, reducing their chances to escape, and in turn, increasing their residence time in the module. Hence, the electric field allows us to increase the time of concentration and enhance the detection signal, making a connection between kinetics and performance.

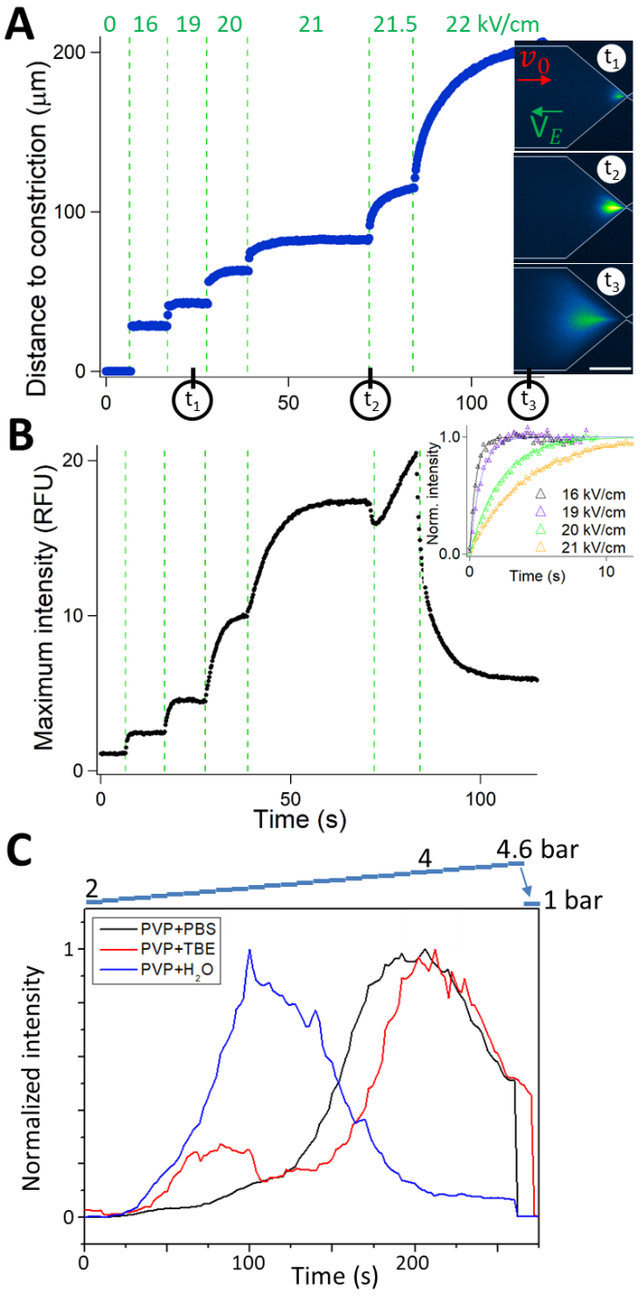

Figure 2: Kinetic response and optimization of the concentration module. (A) *The plot shows the distance of the center of mass of the target:probe (T:P) from the apex as a function of time. We apply a constant pressure associated with* v_0^{max} *of 30 mm/s and a range of electric fields from 0 to 22 kV/cm, as indicated with green vertical dashed lines. The three fluorescence micrographs correspond to snapshots at different time points.* ***(B)*** *The graph presents the maximum fluorescence intensity as a function of time. The inset shows the same fluorescence data normalized in intensity and registered in time for four different electric fields.* ***(C)*** *Normalized fluorescence intensity as a function of time as the pressure is gradually increased from 2 to 4.6 bar as indicated in the upper panel with* E^{max} *set to 20 kV/cm. The viscoelastic solutions were obtained by dissolving PVP in water, electrophoresis buffer, and 0.1X PBS.*

Long targets and short probes enable high sensitivity detection

The technology is expected to concentrate high MW targets more rapidly because they undergo larger transverse forces and can thus be captured with a higher hydrodynamic flow for a given electric field (See Eq. (2)). This hypothesis has been tested by measuring the concentration of four different targets of increasing MW of 44, 98, 114, and 120 nt (see the definition of genomic sequences in Methods). Using the same electrohydrodynamic actuation associated to v_0^{max} and E^{max} of 30 mm/s and 23 kV/cm in a microfluidic chip of 2 µm in height, the maximum intensity after 60 s of actuation increases with the size of the target (Fig. 3A). Moreover, the spatial distribution of concentrated targets becomes more distant from the apex with the size of the target, as indicated by the orange arrow in the snapshots of Fig. 3B. Moreover, the concentration kinetics become slower (Fig. 3C), in agreement with our discussion on the relationship between the time of concentration and the accumulation position (see above). Interestingly, the peak fluorescence signal is enhanced by 27-fold between the 120 and 44 nt target (black and purple curves in Fig. 3A, respectively), and the difference in signal is consistently observed for a broad range of electric fields, as reported in Supplementary Fig. S5.

These experiments also show that the difference of size between the target and the probe is critical to achieve high sensitivity and selective signals. Indeed, the signal of a single strand of 98 nt is 37 % lower than that of a complex formed by pairing 22 nt SP with 92 nt LT, the so-called target of 114 nt (blue and green curves in Fig. 3). Conversely, we do not detect any signal for the 22 nt probe under these actuation conditions (not shown), and collect the maximum signal with the 120 nt complex. Consequently, the concentration module works optimally with a long target of more than ~100 nt and a short hybridization probe of less than ~30 nt.

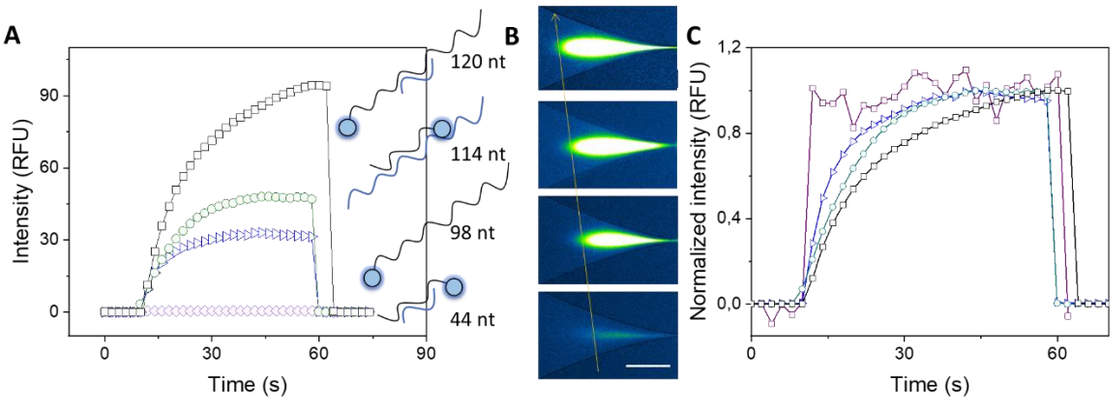

Figure 3. Optimization of target and probe size for biosensing. (A) *The plot shows the concentration kinetics for a series of targets of increasing size of 44, 98, 114, and 120 nt (pink, blue, green and black dataset, respectively).* v_0^{max} *is set to 30 mm/s and* E^{max} *is 23 kV/cm.* ***(B)*** *The fluorescence micrographs correspond to the signal recorded after 50 s of actuation for the 44, 98, 114, and 120 nt targets from bottom to top. The scale bar corresponds to 200 µm.* ***(C)*** *The graph reports the same curves as in (A) after normalization in intensity.*

Grayscale microfluidic chips to enhance the LoD by 100-fold

In our recent study on short targets of 25 nt, we reported an LoD of 2 pM in microchips with a channel height of 2 µm [27]. Here, using the same microfluidic chip, we reach a limit of detection 10-fold enhanced of 0.2 pM with the long target and short probe (blue dataset in Fig. 4A, see details of calculation in Methods). In order to enhance these performances, we aimed to increase the flow rate to accumulate more DNA complexes during the concentration process. For this, we fabricated microfluidic chips of 4 and 6 µm in height. The hydraulic resistance of the chips indeed scales as h^{-3}, implying that the flow rate sharply increases by 26-fold for a 3-fold increase of the channel vertical dimension (Table 1). The electric field is on the other hand less confined at the apex when the height increases, *i.e.* the gradient of voltage is more evenly distributed throughout the chip. E^{max} decreases by 2-fold as h increases from 2 to 6 µm (Table 1). Notably, the scaling of the electrical resistance of h^{-1} is not observed because the contribution of the thick lateral channel cannot be neglected (see size specifications and calculations in Supplementary Material).

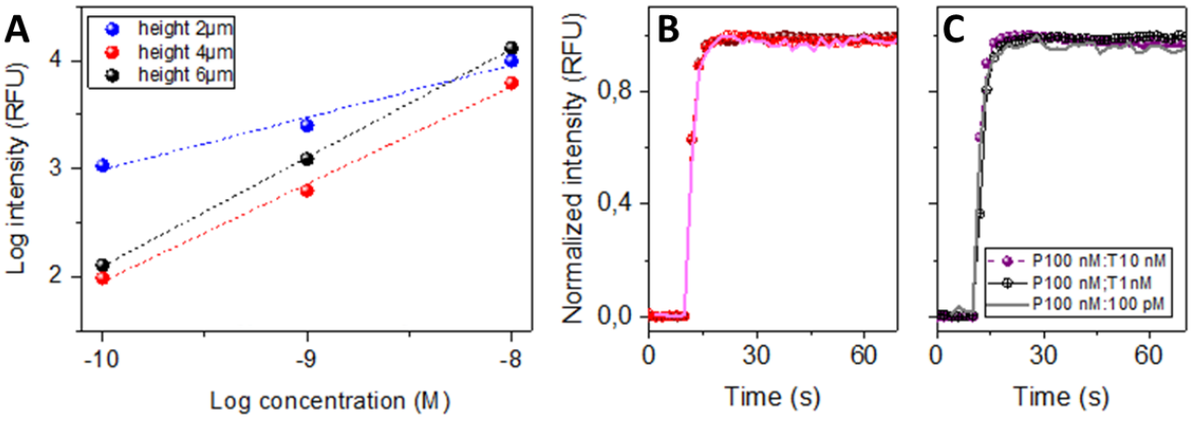

Figure 4. Detection with microfluidic chips of different heights. ***(A)*** *The plot shows the variation of the maximum intensity as a function of target concentration for a channel height of 2, 4, and 6 µm. The probe concentration is set to 100 nM.* ***(B)*** *The graphs represent normalized intensity as a function of time for the three target concentrations of 1, 10, and 100 nM using a microchannel of 4 µm in height.* ***(C)*** *Same as (B) for a channel height of 6 µm. Electrohydrodynamic actuation parameters are specified in Table 1. For the kinetics in 2 µm chips, see* [27].

Using the maximum electric field of 290 V that the oxide layer could withstand, detection is achieved at relatively low pressures of 2 and 1 bar for *h* of 4 and 6 µm, respectively. Despite the possible application of more pressure (our system can deliver 5 bar), the low value of the electric field in these 2D chips (gray lines in Table 1) prevents us from taking advantage of the reduced hydraulic resistance. The resulting electrohydrodynamic actuation parameters v_0^{max} and E^{max} are comparable to that used in the 2 µm chip (Table 1). The kinetics of concentration is rapid with a plateau after ~4 s (Fig. 4B-C), indicating a leaky regime due to the insufficient strength of the electrophoretic force. The LoD of 4 and 5 pM determined for chips of 4 and 6 µm, respectively, *i.e.* an order of magnitude higher than the one obtained with 2 µm chips (Fig. 4A). Albeit the enhanced flow rate in thick microfluidic chips, the electric field becomes limiting to reach a regime of efficient concentration.

In order to deliver high flow rates and high electric fields, we used GSL to produce a channel with a height gradually decreasing from 5.2 to 1.9 µm (Fig. 5A). This geometry indeed enables us to increase v_0^{max} by 40% in comparison to the 2 µm chip (Table 1). Furthermore, the spatial extent of the concentration region, as measured by the intensity profile along the

symmetry axis of the channel (red arrow in Fig. 5A), can be significantly reduced in GSL chips. Setting v_0^{max} to 15, 56, and 51 mm/s, the full width at half maximum decreases from 67, 49 to 24 µm, respectively (light green, dark green, and black curves in Fig. 5B). Moreover, the width of the target band in the 4 µm and 2 µm chips (blue and orange datasets in Fig. 5B, respectively) of 135 µm compare unfavorably to that in the GSL chip. T:P concentration occurs in a region typically reduced by $(135/24)^2$~30 fold, allowing us to reach enhanced detection performances with an LoD of 4 fM (Fig. 5C) *i.e.* three-fold lower compared to our previous report[27]. This performance is explained by the use of long targets and the design of GSL chips, which feature equal gains in sensitivity of 27 and 30-fold, respectively. Furthermore, the dynamic range using the same electrohydrodynamic actuation settings is 5 decades (Fig. 5C), and the concentration kinetics are insensitive to the target concentration (Fig. 5D) with a time scale of 16 s, as inferred from exponential fitting. Notably, the global turnaround time of our assay, including target:probe incubation, sample loading in the chip, and image analysis is on the order of one hour. Nevertheless, our technology appears as a good trade-off between sensitivity and time to result. While a sub-fM level of detection can be achieved by nanosensors [7,8], the response time is on the order of 20 minutes for nanopore, nanowire, cantilever, or surface acoustic wave sensors. Record performances, which feature an LoD of 10^{-17} M in 4 minutes with quartz microbalance [47], 10^{-15} M in 30 s using nanowires [48], or 10^{-15} M in 4 minutes with nanopores [49], compare relatively favorably with our technology.

Let us determine the number of complexes trapped in the concentration module. Given that the flow rate is 0.2 µL/min (Table 1), we expect to process a volume of ~0.1 µL after 30 s of concentration. Therefore, for a target concentration of 20 fM, ~1200 molecules are accumulated in the concentration volume. The background signal is produced by probes at a concentration of 20 nM, which amounts for 1800 molecules in the concentration volume of 23x3.5x1.9 μm^3 (see the characterization of the detection volume Supplementary Fig. S6). The readout signal is indeed equal to 1.8 times the background in our experiment (Supplementary Fig. S7). Taken together, we conclude that GSL chips enable us to enhance detection by nearly 100-fold with no compromise on the concentration kinetics and on the dynamic range, as well as with electric field settings of 190 V that are less prone to induce oxide breakdown.

DNA detection in biological samples (e.g. body fluids [50]) raises complications due to the large amounts of background molecules, which lead to non-specific interactions, as well as to ionic conditions. We already studied whether and to what extent background species in purified and unsalted solutions impaired the detection of our technology[27]. Here, we further investigate that detection using GSL chips operates in unpurified plasma, *i.e.* with a salty solution as well as background protein and nucleic acids. Using equimolar concentrations of target and probes of 20 nM, we spike the running buffer with gradual amounts of plasma of 17, 50, and 100% (Supplementary Fig. S8). Detection is obtained in 17% and 50% plasma-containing solutions with a moderate to an important decrease of the signal by 30% and 60%, respectively. Detection was not achieved in 100% plasma samples due to oxide layer breakdown and irreversible damage of the chip. The salinity of biofluids is a harsh environment for silicon based microfluidic devices due to oxide insulating layer breakdown and to a lesser extent Joule heating. Nevertheless, our results suggest that DNA detection can be operated in plasma provided that the sample is diluted typically five-fold before analysis.

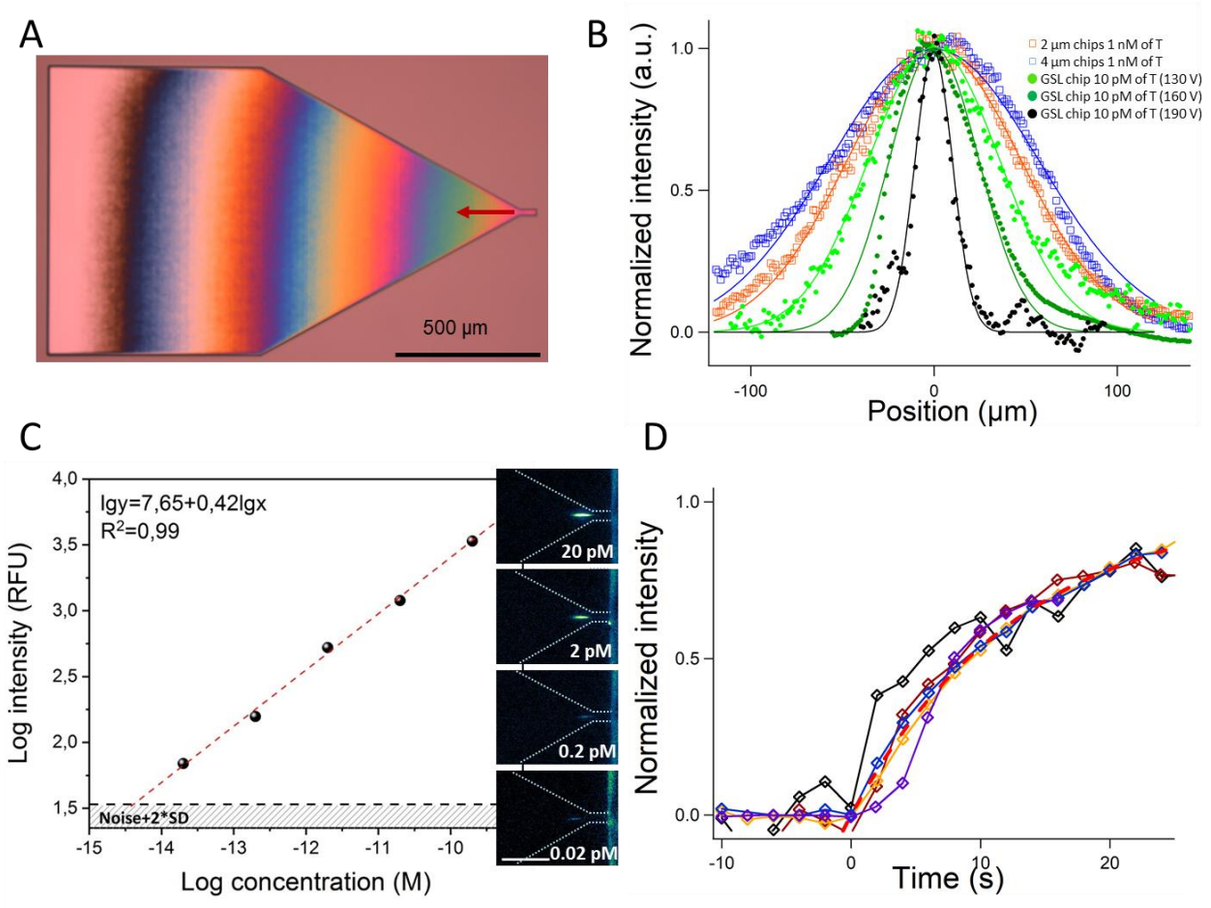

Figure 5. Detection with GSL chips. (A) *Optical micrograph of the GSL chip. The refraction-like pattern arises from the variation in channel height.* ***(B)*** *The graph presents the normalized intensity distribution along the symmetry axis of the channel (red arrow in A) after one minute of concentration for the 2 and 4 µm chips (orange and blue open rectangles, target concentration of 1 nM), as well as for the GSL chip using a tension of 130, 160, and 190 V (light green, dark green and black dots, respectively, target concentration of 10 pM). Note that the peaks of the curves have been registered and centered at 0 for clarity. Solid curves are Gaussian fits.* ***(C)*** *The graph shows the maximum intensity signal after one minute of concentration as a function of the target concentration. The four fluorescence micrographs in the right correspond to snapshots after one minute of concentration (the concentration as indicated in legend).* v_0^{max} *is 51 mm/s and* E^{max} *17 kV/cm.* ***(D)*** *The plot presents the kinetic response of the GSL concentration module for the same five target concentrations as in (C).*

Conclusion

Using GSL to produce an optimized module for nucleic acid concentration, we demonstrate that target DNA molecules of 100 nt or more can be detected with a complementary linear probe of less than 30 nt at an LoD of 4 fM in 30 s. These performances, which are enhanced by three orders of magnitude in comparison to our previous reports, are explained by (i) the use of a long target and short probe that accounts for a 10-fold improved sensitivity, and (ii) the narrow volume of concentration in GSL chips that enables us to obtain 100-fold enhanced signal to noise ratios. As future steps, this technology for biosensing should be tested for concrete biological applications, most notably for cfDNA in oncology applications[50], where background signals are expected to be significantly elevated. cfDNA biosensing could be first tested with abundant genes, such as ALU sequences which are present at concentrations of $60x10^9$ copies/mL[50], so as to delineate the difficulties associated with the use of biofluids and the detection of rare targets. Interestingly, detection sensitivity for rare targets can further be enhanced by integrating strand displacement reactions[15,16] with the concentration module. Whether the strand displacement reaction should be performed before concentration and detection or after concentration of the sample process remains to be clarified in light of the cost in analytical time.

Acknowledgments:

This work was partly supported by the LAAS-CNRS micro and nanotechnologies platform, member of the French RENATECH network. This project was partly supported by the ANR μLAS (ANR-16-CE18-0028-01), the ANR Biopulse (ANR-16-ASTR-0020), and the GRAINE-FEDER PURE-TECH grant.

Data availability statement:

The data that support the findings of this study are available from the corresponding author upon reasonable request.

Supplementary Material

See the supplementary material for details about the computation of hydrodynamic and electric fields, and data about (i) the effect of salt on target:probe intensity (S1), (ii) the fabrication protocol (S2-S3), (iii) the validation of the phase diagram of Fig. 1B (S4), (iv) the detection of targets of different sizes (S5), (v) the spatial characterization of the accumulation region in GSL chips (S6-S7), and (vi) biosensing using diluted and spiked plasma solutions (S8).

References

[1] J. Alcoba-Florez, H. Gil-Campesino, D.G.-M. de Artola, R. González-Montelongo, A. Valenzuela-Fernández, L. Ciuffreda, and C. Flores, Int. J. Infect. Dis. **99**, 190 (2020).
[2] X. Wang, H. Yao, X. Xu, P. Zhang, M. Zhang, J. Shao, Y. Xiao, and H. Wang, Clin. Chem. **66**, 977 (2020).
[3] W. Zhen, E. Smith, R. Manji, D. Schron, and G.J. Berry, J. Clin. Microbiol. **58**, e00783 (2020).
[4] T. Leïchlé, L. Nicu, and T. Alava, ACS Sens. acssensors.0c01463 (2020).
[5] T. Chalklen, Q. Jing, and S. Kar-Narayan, Sensors **20**, 5605 (2020).
[6] J. Tamayo, P.M. Kosaka, J.J. Ruz, Á. San Paulo, and M. Calleja, Chem Soc Rev **42**, 1287 (2013).
[7] M.I.H. Ansari, S. Hassan, A. Qurashi, and F.A. Khanday, Biosens. Bioelectron. **85**, 247 (2016).
[8] D.C. Ferrier, M.P. Shaver, and P.J.W. Hands, Biosens. Bioelectron. **68**, 798 (2015).
[9] T.M. Squires, R.J. Messinger, and S.R. Manalis, Nat. Biotechnol. **26**, 417 (2008).
[10] J.-N. Chuang, P.-Y. Diao, W.-S. Huang, L.-F. Huang, S. Senapati, H.-C. Chang, and Y.-M. Sun, ACS Appl. Mater. Interfaces **12**, 54459 (2020).
[11] M.B. Baker, G. Bao, and C.D. Searles, Nucleic Acids Res. gkr1016 (2011).
[12] G. Garcia-Schwarz and J.G. Santiago, Anal. Chem. **84**, 6366 (2012).
[13] W. Li, W. Jiang, Y. Ding, and L. Wang, Biosens. Bioelectron. **71**, 401 (2015).
[14] Z. Wu, G.-Q. Liu, X.-L. Yang, and J.-H. Jiang, J. Am. Chem. Soc. **137**, 6829 (2015).
[15] C.-P. Liang, P.-Q. Ma, H. Liu, X. Guo, B.-C. Yin, and B.-C. Ye, Angew. Chem. Int. Ed. **56**, 9077 (2017).
[16] C.Y. Song, Y.J. Yang, B.Y. Yang, Y.Z. Sun, Y.P. Zhao, and L.H. Wang, Nanoscale **8**, 17365 (2016).
[17] G. Wang, M. Yu, and G. Wang, Biosens. Bioelectron. **138**, 111319 (2019).
[18] H. Wu, Y. Liu, H. Wang, J. Wu, F. Zhu, and P. Zou, Biosens. Bioelectron. **81**, 303 (2016).
[19] S.W. Shin, S.Y. Ahn, Y.T. Lim, and S.H. Um, Anal. Chem. **91**, 14808 (2019).
[20] S.S. Bahga, C.M. Han, and J.G. Santiago, The Analyst **138**, 87 (2013).
[21] M. Bercovici, C.M. Han, J.C. Liao, and J.G. Santiago, Proc. Natl. Acad. Sci. **109**, 11127 (2012).
[22] A. Persat and J.G. Santiago, Anal. Chem. **83**, 2310 (2011).
[23] R. Malbec, B. Chami, L. Aeschbach, G.A. Ruiz Buendía, M. Socol, P. Joseph, T. Leïchlé, E. Trofimenko, A. Bancaud, and V. Dion, Sci. Rep. **9**, 23 (2019).
[24] N. Milon, J.-L. Fuentes Rojas, A. Castinel, L. Bigot, G. Bouwmans, K. Baudelle, A. Boutonnet, A. Gibert, O. Bouchez, C. Donnadieu, F. Ginot, and A. Bancaud, Lab. Chip **20**, 175 (2020).
[25] H. Ranchon, R. Malbec, V. Picot, A. Boutonnet, P. Terrapanich, P. Joseph, T. Leïchlé, and A. Bancaud, Lab. Chip **16**, 1243 (2016).
[26] N. Milon, C. Chantry-Darmon, C. Satge, M.-A. Fustier, S. Cauet, S. Moreau, C. Callot, A. Bellec, T. Gabrieli, and L. Saïas, Nucleic Acids Res. **47**, 8050 (2019).

[27] I. Tijunelyte, R. Malbec, B. Chami, J. Cacheux, C. Dez, T. Leichlé, P. Cordelier, and A. Bancaud, Biosens. Bioelectron. **178**, 112992 (2021).
[28] S.-H. Song, K. Kim, S.-E. Choi, S. Han, H.-S. Lee, S. Kwon, and W. Park, Opt. Lett. **39**, 5162 (2014).
[29] A.M. Bowen, J.A. Ritchey, J.S. Moore, and R.G. Nuzzo, Small **7**, 3350 (2011).
[30] Y. Ouyang, S. Wang, J. Li, P.S. Riehl, M. Begley, and J.P. Landers, Lab. Chip **13**, 1762 (2013).
[31] A. Naillon, H. Massadi, R. Courson, J. Bekhit, L. Seveno, P.F. Calmon, M. Prat, and P. Joseph, Microfluid. Nanofluidics **21**, 131 (2017).
[32] A. Naillon, C. de Loubens, W. Chèvremont, S. Rouze, M. Leonetti, and H. Bodiguel, Phys. Rev. Fluids **4**, 053301 (2019).
[33] F. Del Giudice, G. Romeo, G. D'Avino, F. Greco, P.A. Netti, and P.L. Maffettone, Lab. Chip **13**, 4263 (2013).
[34] C.T. Rueden, J. Schindelin, M.C. Hiner, B.E. DeZonia, A.E. Walter, E.T. Arena, and K.W. Eliceiri, BMC Bioinformatics **18**, 529 (2017).
[35] C.-F. Chou, J.O. Tegenfeldt, O. Bakajin, S.S. Chan, E.C. Cox, N. Darnton, T. Duke, and R.H. Austin, Biophys. J. **83**, 2170 (2002).
[36] I.-F. Cheng, S. Senapati, X. Cheng, S. Basuray, H.-C. Chang, and H.-C. Chang, Lab. Chip **10**, 828 (2010).
[37] B.J. Sanghavi, W. Varhue, J.L. Chávez, C.-F. Chou, and N.S. Swami, Anal. Chem. **86**, 4120 (2014).
[38] S. Li, Z. Ye, Y.S. Hui, Y. Gao, Y. Jiang, and W. Wen, Biomicrofluidics **9**, 054115 (2015).
[39] F. Camacho-Alanis, L. Gan, and A. Ros, Sens. Actuators B Chem. **173**, 668 (2012).
[40] R.C. Gallo-Villanueva, C.E. RodrÃ-guez-LÃ³pez, R.I. DÃ-az-de-la-Garza, C. Reyes-Betanzo, and B.H. Lapizco-Encinas, ELECTROPHORESIS **30**, 4195 (2009).
[41] M. Socol, H. Ranchon, B. Chami, A. Lesage, J.-M. Victor, M. Manghi, and A. Bancaud, Macromolecules **52**, 1843 (2019).
[42] R.J. Montes, A.J. Ladd, and J.E. Butler, Biomicrofluidics **13**, 044104 (2019).
[43] B. Chami, M. Socol, M. Manghi, and A. Bancaud, Soft Matter **14**, 5069 (2018).
[44] O. Schnitzer and E. Yariv, J. Fluid Mech. **786**, 84 (2016).
[45] J. Klein, Annu. Rev. Mater. Sci. **26**, 581 (1996).
[46] M. Arca, A.J. Ladd, and J.E. Butler, Soft Matter **12**, 6975 (2016).
[47] Z. Mo, H. Wang, Y. Liang, F. Liu, and Y. Xue, The Analyst **130**, 1589 (2005).
[48] A. Gao, N. Lu, Y. Wang, P. Dai, T. Li, X. Gao, Y. Wang, and C. Fan, Nano Lett. **12**, 5262 (2012).
[49] M. Wanunu, T. Dadosh, V. Ray, J. Jin, L. McReynolds, and M. Drndić, Nat. Nanotechnol. **5**, 807 (2010).
[50] R. Malbec, J. Cacheux, P. Cordelier, T. Leichlé, P. Joseph, and A. Bancaud, Micro Nano Eng. **1**, 25 (2018).

Biomicrofluidics

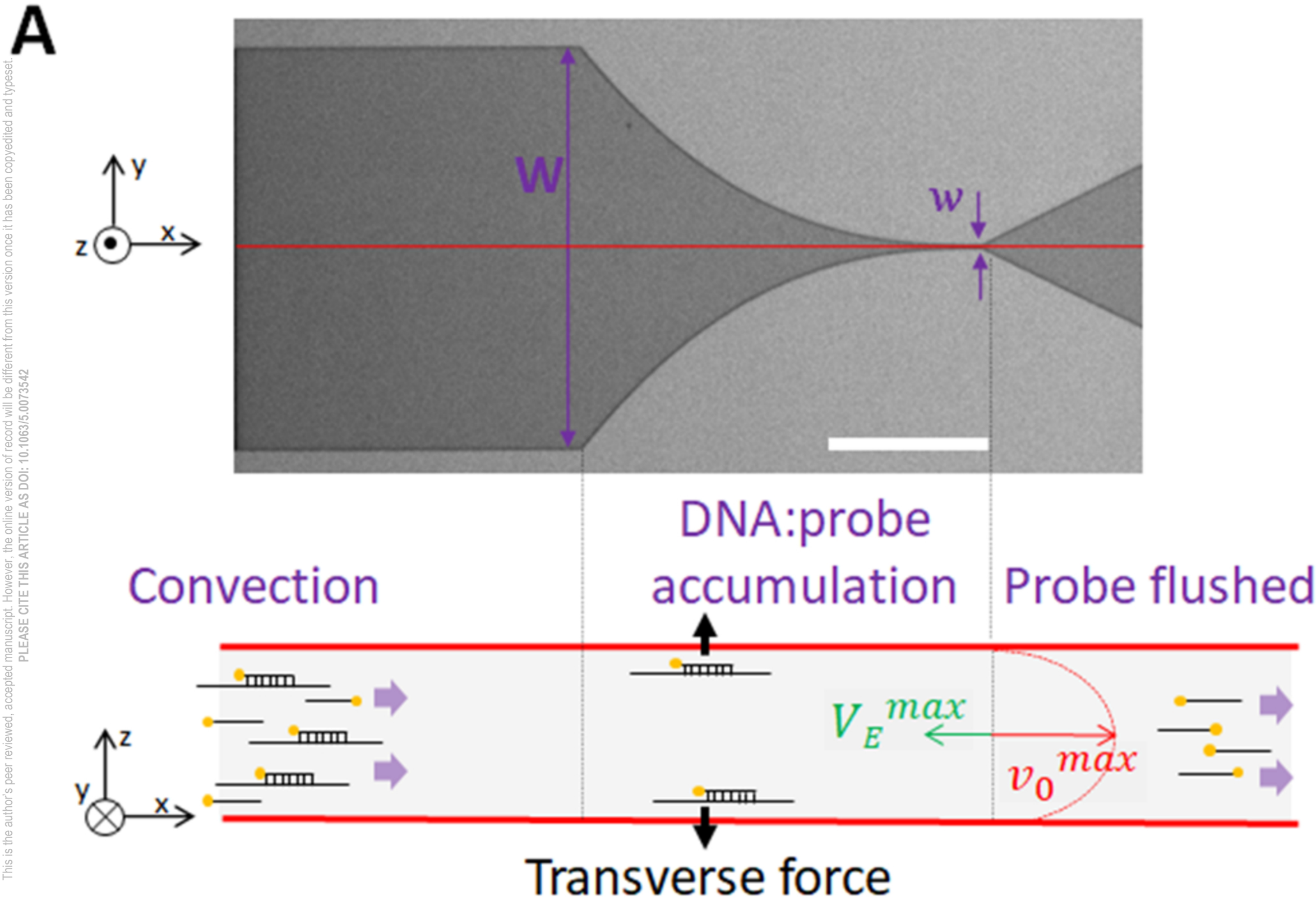

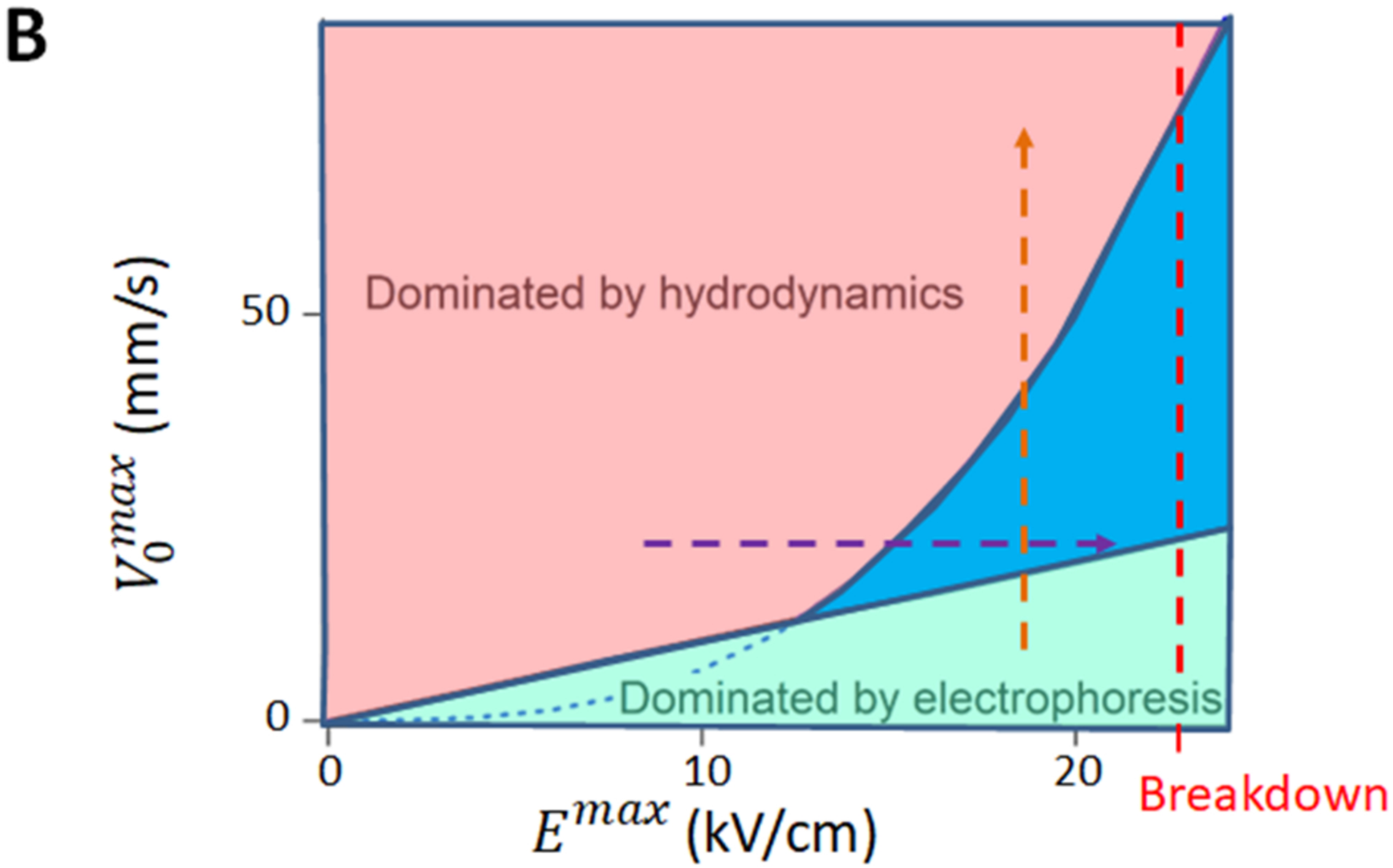

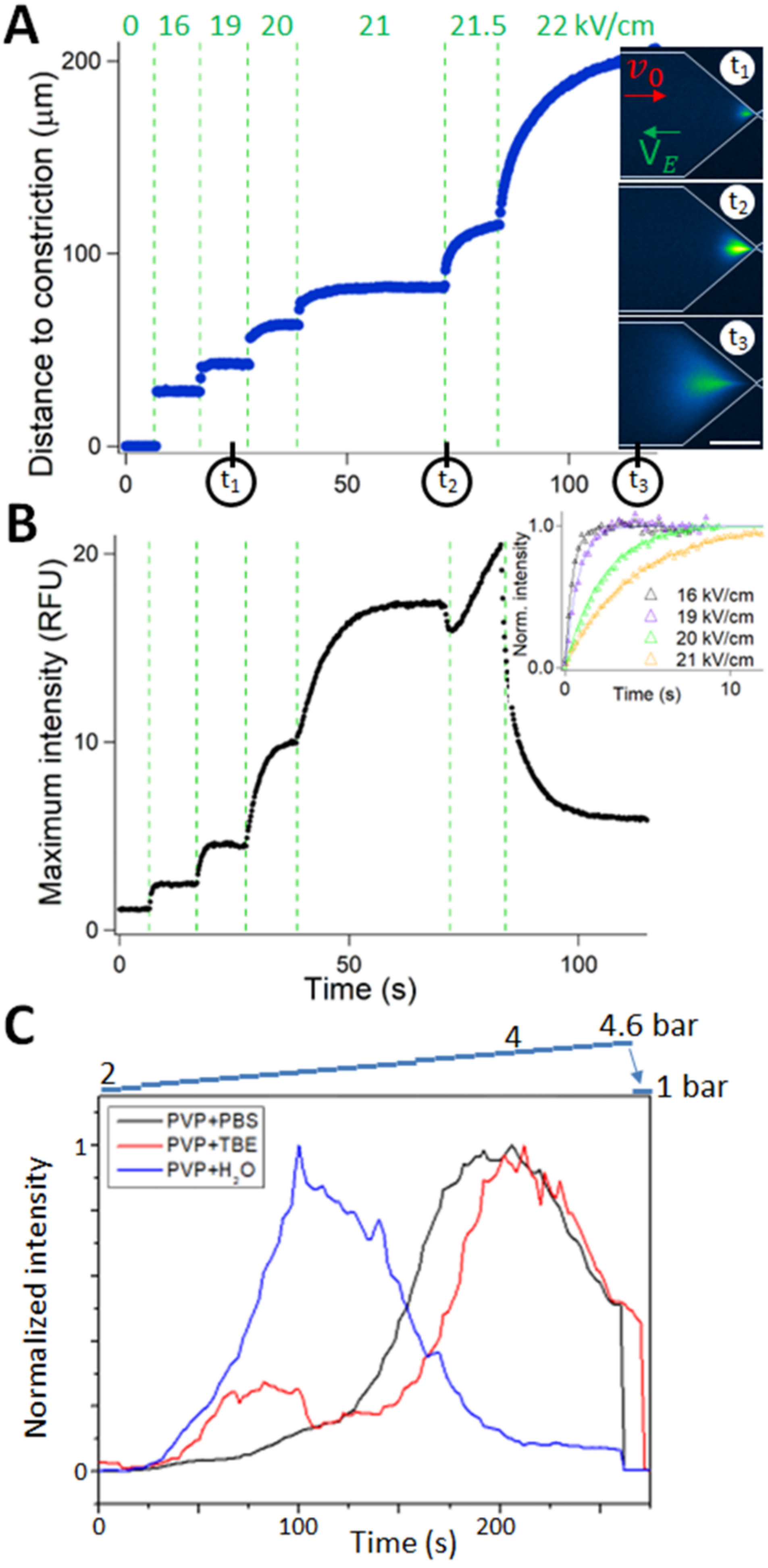

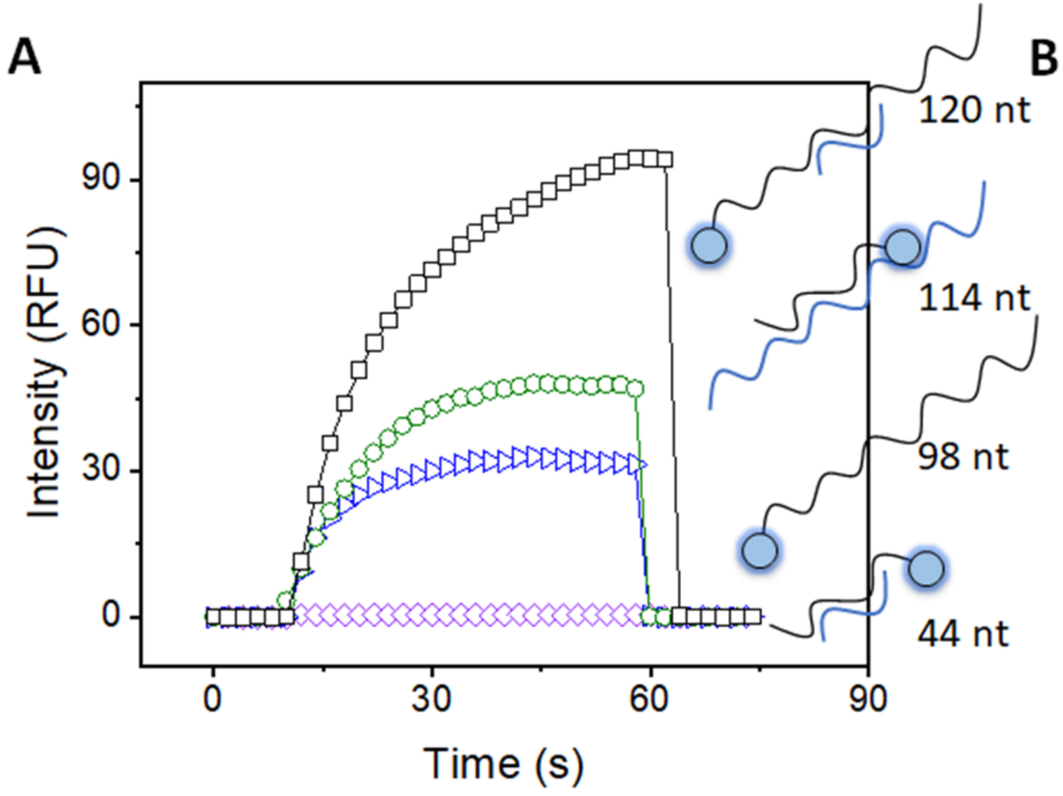

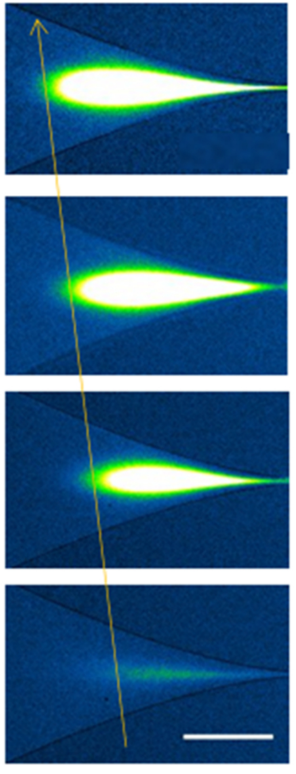

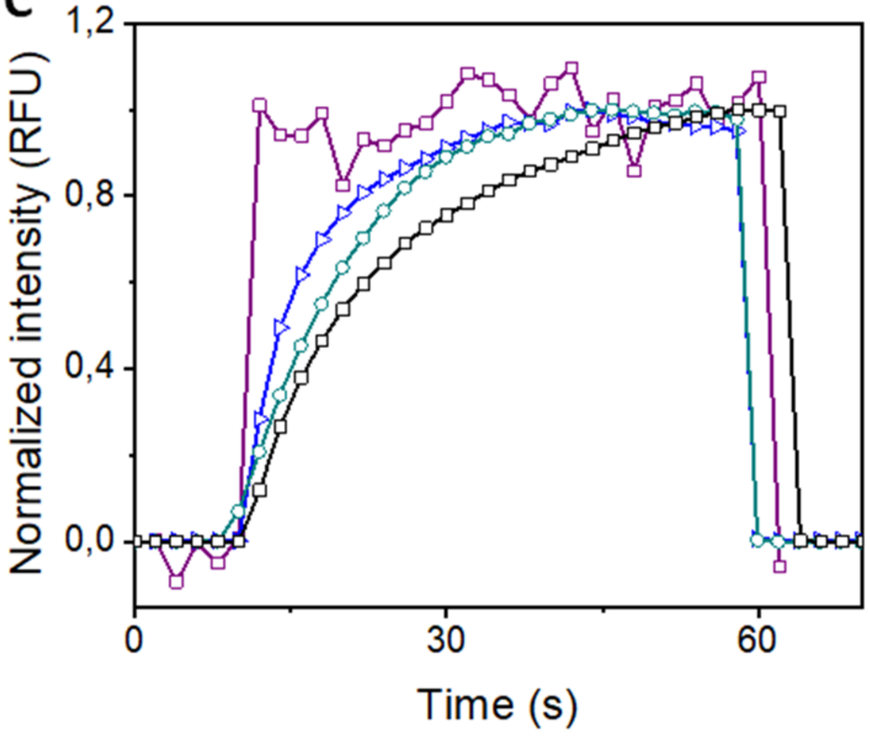

Biomicrofluidics